Tensile response of AP-PLY composites: a multiscale experimental and numerical study

Citation for published version:
Kok, R, Martinez-Hergueta, F & Teixeira-Dias, F 2022, 'Tensile response of AP-PLY composites: a multiscale experimental and numerical study', *Composites Part A: Applied Science and Manufacturing*, vol. 159, 106989. https://doi.org/10.1016/j.compositesa.2022.106989

Digital Object Identifier (DOI):
10.1016/j.compositesa.2022.106989

Published In:
Composites Part A: Applied Science and Manufacturing

Tensile response of AP-PLY composites: a multiscale experimental and numerical study

Rutger Kok, Francisca Martinez-Hergueta*, Filipe Teixeira-Dias

School of Engineering, Institute for Infrastructure and Environment, The University of Edinburgh, William Rankine Building, Edinburgh EH9 3FG, UK

**francisca.mhergueta@ed.ac.uk*

Abstract

This study presents the experimental and numerical characterization of composite laminates manufactured using a novel method known as Advanced Placed Ply (AP-PLY). The behavior of cross-ply and quasi-isotropic AP-PLY laminates under uniaxial tension is compared with that of baseline laminates. Stiffness is found to be unaffected by the preforming process, while the strength is dependent on the laminate configuration. A 3D multiscale numerical modeling framework is developed to capture the effect of the through-thickness fiber undulations present in the AP-PLY composites. The ability of the framework to accurately predict the stress-strain behavior and failure mechanisms at a relatively low computational cost is demonstrated. The approach is also exploited to investigate the influence of design parameters and improve the strength of the laminates. These results show the potential of the numerical framework to optimize the fiber placement preforming process to design AP-PLY components for structural applications.

Keywords: Computational modeling, Damage mechanics, Automated Fiber Placement (AFP), 3-Dimensional reinforcement

1. Introduction

Automated Fiber Placement (AFP) is an emerging technique to manufacture advanced composites for the aerospace industry. One of its main advantages is the possibility to define complex fiber paths to optimize the stiffness for a given loading scenario [1, 2, 3, 4]. One example of AFP three-dimensional reinforcement is AP-PLY (or Advanced Placed Ply), a novel strategy to produce pseudo-woven structures with improved impact resistance. Compared with existing methods for impact tolerance improvement, such as z-pinning or 3D weaving, AP-PLY preforming does not result in fiber breakage and introduces only minimal fiber crimp, allowing AP-PLY laminates to retain the excellent undamaged in-plane strength and stiffness of conventional angle-ply laminates [5].

The first investigations of AP-PLY laminates were performed by Nagelsmit, who reported a significant improvement in the mode I interlaminar fracture toughness (89.2%) and the compression after impact (CAI) strength (15%) relative to conventional laminates [6]. These conclusions are echoed in a number of more recent studies [7, 8, 9, 10, 11, 12]. The majority of the existing studies have been primarily experimental in focus. Although 2D analytical and numerical models have been developed to estimate stiffness and delamination [6, 13, 14], their capacity to predict the 3D stress-strain response of complex AP-PLY composites with multiple tow orientations is limited. The development of numerical models for damage tolerance analysis is a first step to provide thorough insight into the failure micro-mechanisms of this family of composites and to facilitate their adoption in structural applications. The primary challenge lies in the replication of the complex geometries of AP-PLY laminates at a reasonable computational cost.

AP-PLY laminates with only two orthogonal tow orientations are essentially woven laminates, and as such their geometries can be generated relatively easily with software packages such as TexGen or WiseTex [15, 16]. As the number of tow orientations in an AP-PLY laminate rises, however, their internal architecture becomes increasingly complex and cannot be easily replicated using textile geometry creation packages, which are based on two dimensional Bézier splines. Moreover, these approaches use simplified yarn shapes, are subject to tow interpenetration issues, and are costly and time consuming to adapt to AP-PLY composites [17, 18].

Rad *et al.* modeled the tensile response of quasi-isotropic AP-PLY composites using an elastic 3D shell model. The model does not, however, account for the effect of through-thickness fiber undulations, a limitation which the authors acknowledge inhibits the accuracy of their model predictions [10]. More recently, Li *et al.* developed a software package to generate 3D geometries of AP-PLY laminates [18]. A subsequent study by Li *et al.* utilized their tow-based modeling strategy to predict the behavior of two different types of AP-PLY composites to three point bending [19]. While the generated geometries show good agreement with micrographs of manufactured laminates, and the correlation between the experimental and numerical results is good, the computational cost of the model is significant, and it is still subject to interpenetration issues when the mesh is not sufficiently refined [18]. Moreover, since the model uses cohesive interactions to capture matrix cracking, rather than a continuum damage mechanics or XFEM approach, arbitrary crack paths cannot be captured. Finally, the lack of a fiber failure criteria limits the ability of the numerical model to simulate load cases where interlaminar damage is not the primary damage mechanism.

The aim of this paper is to provide a comprehensive study of the tensile response of AP-PLY laminates and develop a multiscale simulation framework for structural design of components manufactured using AFP. In this study, the in-plane response of two different AP-PLY configurations is studied. The mechanical properties of the AP-PLY composites are compared with conventional angle-ply laminates to quantify the effect of the preforming process on the undamaged in-plane strength and stiffness of the laminates. A 3D multiscale numerical framework is developed to efficiently capture the effect of through-thickness fiber undulations. The predictive capability, computational cost, and limitations of the approach are analyzed. Consequently, the numerical framework is exploited to investigate the influence of manufacturing parameters on the mechanical response of the AP-PLY composites.

2. Materials and methods

Two AP-PLY laminates with different internal architectures were manufactured: (i) a cross-ply laminate $[0/90]_{2s}$ ($XP_{\text{AP-PLY}}$) and (ii) a quasi-isotropic laminate with stacking sequence $[0/45/90/\text{-}45]_s$ ($QI_{\text{AP-PLY}}$). The latter represents the state of the art in terms of the complexity of its internal architecture [11, 9, 7]. The AP-PLY panels were laid up by hand in a process emulating automated fiber placement. Tows were cut out of a roll of prepreg (SHD Composites VTC401) to a width of 10 mm, then placed into a mold in a predefined sequence. Guides were used to ensure correct alignment. Figure 1 illustrates the layup process for the quasi-isotropic AP-PLY laminate. In both laminates a gap of three tow widths was left between tows placed in the same pass, as in [10, 12]. The 300×300 [mm^2] panels were cured in a hot press under 4 bars of pressure at 120°C for 120 minutes. In addition, two reference — non AP-PLY — laminates were manufactured for comparison with the AP-PLY panels, (XP_{ref} and QI_{ref}). The discrepancies between the thicknesses of the AP-PLY and baseline specimens were negligible. The average thicknesses of the cross-ply AP-PLY and baseline specimens were 1.68 mm and 1.63 mm respectively. The quasi-isotropic AP-PLY and baseline thicknesses were 1.61 mm and 1.63 mm. A fiber volume fraction of approximately 53.2% was obtained for all the laminates. Glass fiber end tabs were adhered to all specimens using an epoxy adhesive film (SHD Composites VTFA400).

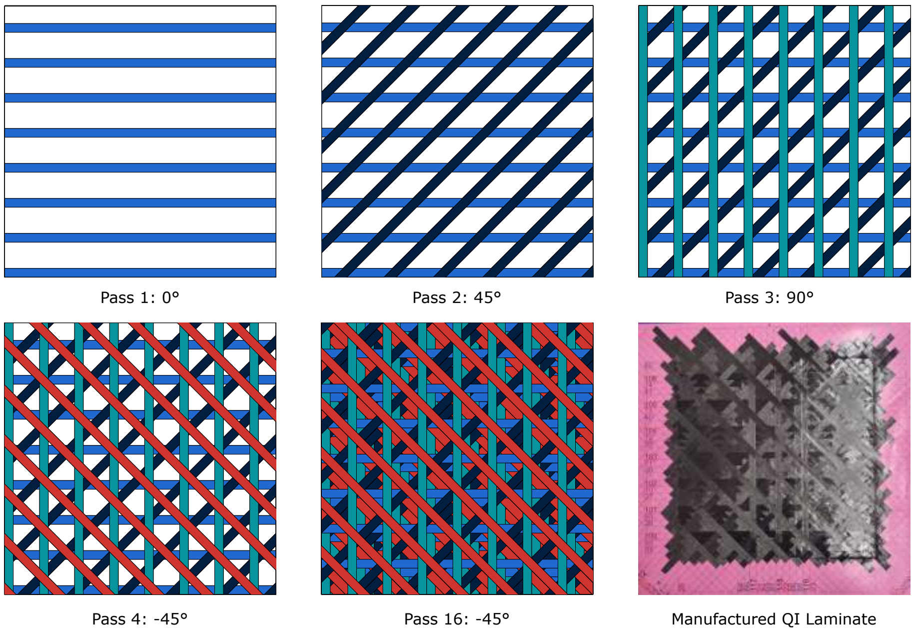

Figure 1: Layup process for a quasi-isotropic AP-PLY laminate. Note layup steps 5-15 are omitted for brevity.

Specimens were extracted using a water cooled diamond saw. The dimensions of the baseline specimens conformed to the ISO 527 standard (25×250 [mm^2] with 50 mm long end tabs). However, the AP-PLY specimens had larger dimensions (40×300 [mm^2] with 100 mm long end tabs) to ensure their mechanical response was representative of the behavior of their parent laminates. As discussed in the work of Rad *et al.* certain AP-PLY laminate configurations, including the quasi-isotropic AP-PLY laminate in this study, do not contain a well defined representative volume element (RVE)

[10]. Where an RVE is not readily identifiable, an "approximate" RVE can be determined. In the case of the QI AP-PLY specimens, this approximate RVE measures 40×40 [mm^2].

The tensile characterization was carried out in accordance with the ISO 527 standard. Six specimens from each panel were tested using an MTS 300 kN universal testing machine, at 2 mm/min cross-head displacement. Full-field displacements were recorded using a 2D digital image correlation system, with post-processing conducted using the VIC-2D software package. The laminates were inspected using a Hitachi TM4000Plus Scanning Electron Microscope (SEM).

3. Multiscale Numerical Modeling

The model presented in this section describes the mechanical response of AP-PLY laminates including the mechanical response of the tow undulations created by the preforming process. The role of the through-thickness reinforcement is critical to the accurate prediction of deformation, failure and damage progression in 3D composites [20, 10]. Modeling the tow undulations explicitly as solid continua is challenging due to the complexity of their internal architecture at non-orthogonal tow crossovers. Moreover, this approach is subject to tow interpenetration issues, which may require manual intervention to resolve [18]. In this study, a new approach is proposed in which the macroscale variations in strength and stiffness resulting from the presence of tow undulations are captured through the use of multiscale modeling.

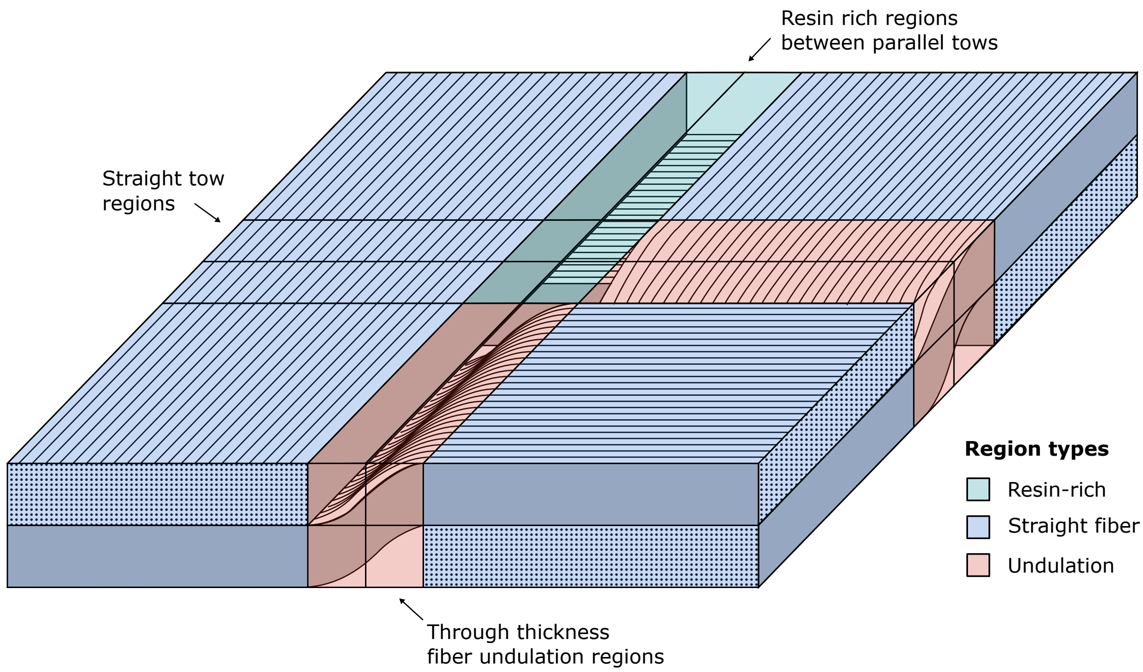

Figure 2: Illustration of the idealized geometry used in the numerical models.

AP-PLY laminates are first divided into regions of three different types: straight fiber, undulation and resin-rich regions. Figure 2 illustrates schematically the idealized geometry of a cross-ply AP-PLY laminate divided in such a manner. The elements in each region are assigned the material properties, volume fractions, and orientations of their constituents. Resin-rich regions, for

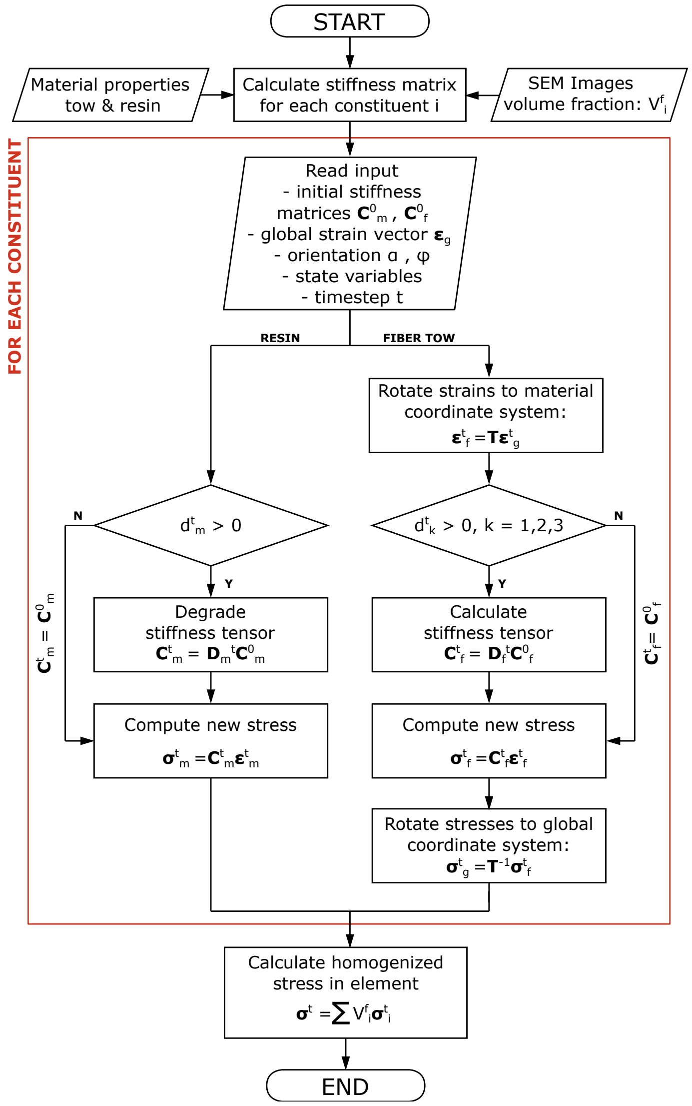

Figure 3: Flowchart illustrating the multiscale algorithm for 3D damage modeling in AP-PLY composites. The t superscript denotes the time step (0 indicates the initial time step). The $\mathbf{D}$ variable represents the damage matrix.

example, consist of a non-undulating tow and a neat resin pocket. The elements in each region function as mesoscale unit cells. In this manner, the effects of through-thickness undulations can be captured without modeling curved fiber paths geometrically.

The global strain state at each integration point, as determined through the macroscale model, is provided as input to the multiscale algorithm. The strains on each constituent at the mesoscale (in the element coordinate system) are assumed to be equal to the global strains through an iso-strain assumption [21]. This assumption is reasonable given the in-plane loading and the relatively small out-of-plane fiber orientations encountered in AP-PLY laminates. However, care should be taken when extending this approach to laminates with higher fiber curvatures, large heterogeneities, or load cases which stress the material primarily in the through thickness direction. The strains in the global coordinate system are subsequently transformed to the material coordinate system for each of the mesoscale orthotropic constituents (this operation is not performed for the resin constituent). The stresses in each constituent — in the the material coordinate system — are then

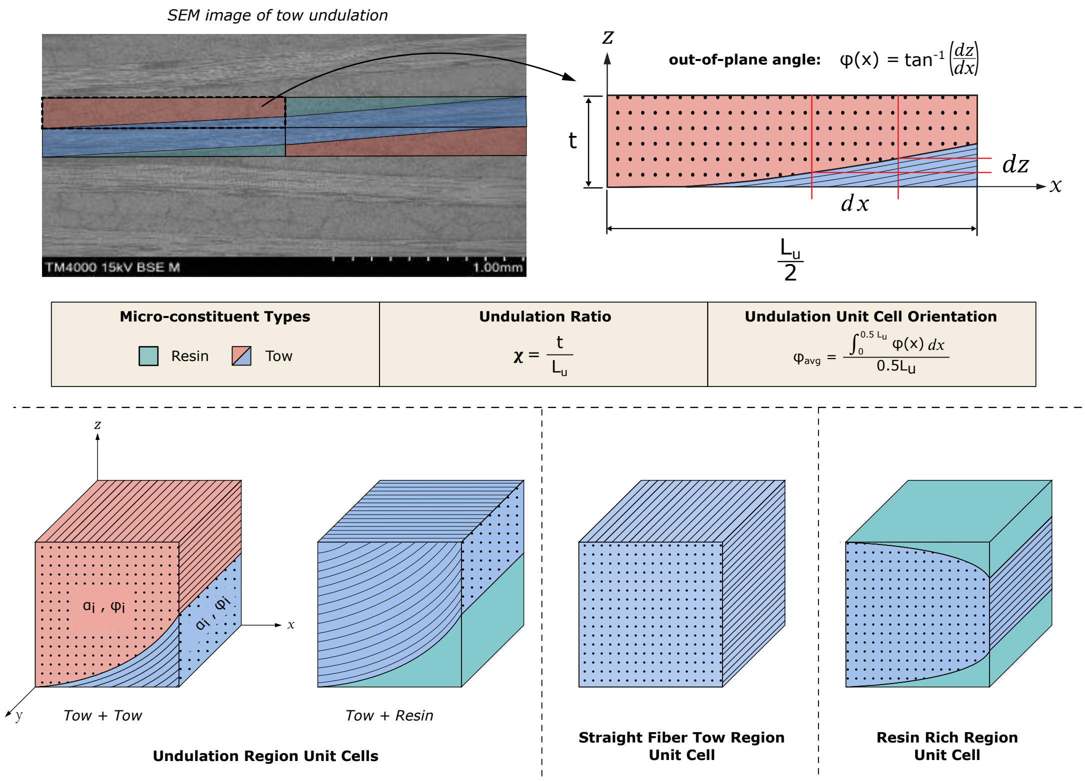

Figure 4: Schematic of the unit cells for the different region types.

determined using the appropriate constitutive model (see Sections 3.2 and 3.3). This approach separately captures the initiation and evolution of damage in each constituent. Once the stresses in each constituent have been determined they are rotated back to the global coordinate system. The homogenized stress on each element can then be calculated through volumetric averaging of the stresses in each constituent. A flowchart summarizing the modeling methodology can be found in Figure 3.

3.1. Microscale model

Unit cells are defined to represent the region types (straight tow, undulation, or resin rich) identified in Figure 2. Depending on the region they represent, the unit cells contain differing proportions of fiber tow and pure resin micro constituents, see Figure 4. In addition, the fiber tow micro constituents in each unit cell possess an in-plane and out-of-plane orientation.

The simplest of these representative volume elements is the straight fiber tow unit cell, which does not contain any pure resin pockets, and whose fibers are all aligned in the plane. Resin rich unit cells represent the edges of tows where the fiber volume fraction is comparatively low, consisting of a pure resin and straight tow constituents. Lastly, through thickness tow undulations are modeled through the combination of four geometrically congruent unit cells, as illustrated in Figure 4. Each unit cell contains either an undulating tow and a resin pocket, or two tows with differing in-plane and out-of-plane orientations.

The stress-strain response of the tow and resin micro-constituents are governed by their respective material models, described in Sections 3.2 and 3.3. In the case of the tow constituents, the global macroscale strain is transformed into the material coordinate system defined by the in-plane ply angle (α) and the average out-of-plane orientation (φ_{avg}), as defined in Figure 4. Note that since the pure resin regions are isotropic, strains in these regions do not need to be transformed.

3.2. Constitutive behavior: fiber tows

Damage in the impregnated fiber tows is defined by a continuum damage mechanics framework that degrades the stiffness of the material as damage accumulates based on the models developed by Maimi *et al.* and Shah *et al.* [22, 23, 21].

Material behavior prior to failure is linear-elastic. After the onset of damage, the gradual unloading of a ply is simulated according to damage evolution laws expressed as function of three damage variables: d_1, representing longitudinal fiber damage, d_2, representing transverse damage in the plane of the ply, and d_3 representing out-of-plane damage. All damage variables are equal to zero prior to damage initiation, and increase to unity at strains corresponding to failure. The compliance tensor of the material can be expressed as a function of the damage variables and the elastic constants of the material as:

$$\mathbf{H} = \begin{bmatrix} \frac{1}{(1-d_1)E_1} & -\frac{v_{12}}{E_1} & -\frac{v_{12}}{E_1} & 0 & 0 & 0 \\ -\frac{v_{12}}{E_1} & \frac{1}{(1-d_2)E_2} & -\frac{v_{23}}{E_2} & 0 & 0 & 0 \\ -\frac{v_{12}}{E_1} & -\frac{v_{23}}{E_2} & \frac{1}{(1-d_3)E_2} & 0 & 0 & 0 \\ 0 & 0 & 0 & \frac{1}{(1-d_1)(1-d_2)G_{12}} & 0 & 0 \\ 0 & 0 & 0 & 0 & \frac{1}{(1-d_2)(1-d_3)G_{23}} & 0 \\ 0 & 0 & 0 & 0 & 0 & \frac{1}{(1-d_1)(1-d_3)G_{31}} \end{bmatrix} \tag{1}$$

To ensure mesh objectivity, the constitutive model employs the crack band model proposed by Bazant and Oh, in which the energy dissipated by an element is regularized using its characteristic length [24]. The characteristic lengths of each micro-constituent, i, were defined as the cubic root of each their volume $V_{\rm i}$, which means the most accurate results are obtained using elements with an aspect ratio close to one [25, 26].

$$\ell = \sqrt[3]{V_{\rm i}} \tag{2}$$

$$g_{\rm M}^{\rm k} = \frac{\mathcal{G}_{\rm M}^{\rm k}}{\ell}; \quad M = 1, 2, 3; \quad {\rm k} = {\rm T}, {\rm C} \tag{3}$$

where $\mathcal{G}_{\rm M}^{\rm k}$ is the fracture toughness of the material along the loading direction M, adjusted to account for the volume fraction of the constituent in the unit cell. In other words, the volumetric fracture energy density is calculated by dividing the fracture toughness of the relevant material by its characteristic length — the cubic root of the volume of the corresponding constituent. $g_M^{\rm k}$ is the energy dissipated per unit volume, T and C denote tensile and compressive loads, respectively, and ℓ is the characteristic length of the constituent. The strain-softening relationships for fiber and matrix damage modes are illustrated in Figure 5.

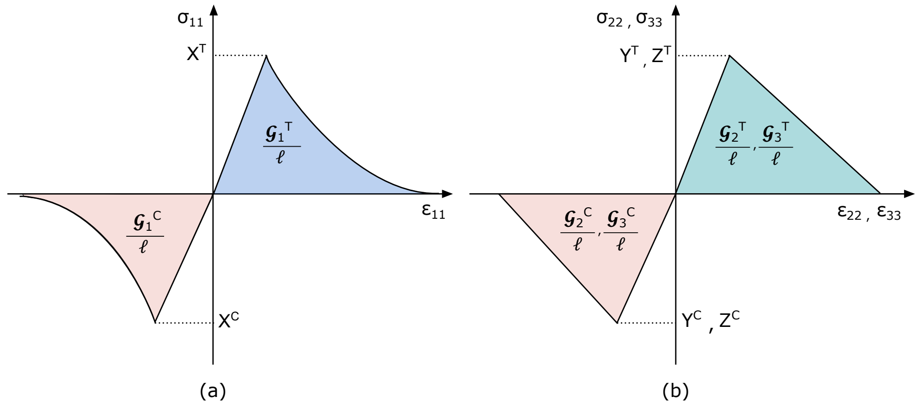

Figure 5: Longitudinal (a) and transverse or through-thickness (b) stress–strain response.

The initiation of damage under longitudinal loading is governed by simple non-interactive maximum strain criteria F_1^{T} and F_1^{C}:

$$F_1^{\mathrm{k}} = \frac{\varepsilon_{11}}{\varepsilon_{11}^{0\mathrm{k}}}; \quad \mathrm{k} = \mathrm{T}, \mathrm{C} \tag{4}$$

where $\varepsilon_{11}^{0\mathrm{k}}$ represents the strain corresponding to the strength of the material, i.e. $\varepsilon_{11}^{OC} = X^{\mathrm{C}}/E_{11}$. After the onset of damage, the stiffness of the material is degraded according to a scalar damage variable d_1^{k}, defined by an exponential law. In tension, the exponential law is given by Equation 5.

$$d_1^{\mathrm{T}} = 1 - \frac{1}{r_1^{\mathrm{T}}} \exp\left[A_1^{\mathrm{T}}\left(1 - r_1^{\mathrm{T}}\right)\right] \tag{5}$$

where r_1^{T} is the longitudinal tensile elastic domain threshold, initially equal to one and increasing monotonically with damage evolution. The tensile elastic domain threshold is a function of both the tensile and compressive failure criteria. This is because cracks that form under compressive loading open on load reversal [22].

$$r_1^{\mathrm{T}} = \max\left\{1, \max_{s=0,t}\left\{F_1^{\mathrm{T}}\right\}, \max_{s=0,t}\left\{F_1^{\mathrm{C}}\right\}\right\} \tag{6}$$

where s denotes a single time step, in the range from 0 to t, and t is the current time step. A_1^{T} is a parameter that ensures the correct dissipation of fracture energy and is a function of the characteristic length in the fiber direction ℓ_{fib}. E_{11} is the Young's modulus in the fiber direction, $\mathcal{G}_1^{\mathrm{T}}$ is the longitudinal tensile fracture energy, and X^{T} is the longitudinal tensile strength.

$$A_1^{\mathrm{T}} = \frac{2\ell_{\mathrm{fib}}\left(X^{\mathrm{T}}\right)^2}{2E_{11}\mathcal{G}_1^{\mathrm{T}} - \ell_{\mathrm{fib}}\left(X^{\mathrm{T}}\right)^2} \tag{7}$$

In compression, the damage variable d_1^{C} must be expressed as a function of both the longitudinal damage variable d_1^{T} and the compressive elastic domain threshold r_1^{C}. While cracks formed under tensile loading will close under compressive loads, the broken and misaligned fibers cannot carry any additional load [23].

$$d_1^{\mathrm{C}} = 1.0 - (1.0 - d_1^{\mathrm{C}*})(1.0 - A_1^{\pm} d_1^{\mathrm{T}}) \tag{8}$$

where $d_1^{\mathrm{C}*}$ is the exponential damage evolution function for purely compressive damage, given by Equation 9.

$$d_1^{\mathrm{C}*} = 1 - \frac{1}{r_1^{\mathrm{C}}} \exp\left[A_1^{\mathrm{C}}\left(1 - r_1^{\mathrm{C}}\right)\right] \tag{9}$$

Note that since the tensile cracks close under load reversal the compressive elastic domain threshold is not affected by tensile damage, see Equation 10. The A_1^{C} is defined in the same fashion as in the tensile mode.

$$r_1^{\mathrm{C}} = \max\left\{1, \max_{s=0,t}\left\{F_1^{\mathrm{C}}\right\}\right\} \tag{10}$$

$$A_1^{\mathrm{C}} = \frac{2\ell_{\mathrm{fib}}\left(X^{\mathrm{C}}\right)^2}{2E_{11}\mathcal{G}_1^{\mathrm{C}} - \ell_{\mathrm{fib}}\left(X^{\mathrm{C}}\right)^2} \tag{11}$$

The $A_1^{\pm}$ parameter defines the extent to which damage accumulated in tension affects the compressive response

$$A_1^{\pm} = b\frac{E_{11} - E_{22}}{E_{11}} \tag{12}$$

where E_{11} and E_{22} are the longitudinal and transverse moduli of a lamina. The b parameter is used to control the extent of stiffness retention. When $b = 1$, the loads are assumed to be carried solely by the matrix. When $b = 0$ fibers are assumed not to have lost alignment and there is no loss in stiffness. In the present work, an intermediate value of 0.5 has been used.

Finally, the longitudinal damage variable d_1 can be expressed as a function of the tensile and compressive damage variables and the sign of the longitudinal normal stress. This accounts for the closure of cracks occurring under load reversal.

$$d_1 = d_1^{\mathrm{T}}\frac{\langle\sigma_{11}\rangle}{|\sigma_{11}|} + d_1^{\mathrm{C}}\frac{\langle-\sigma_{11}\rangle}{|\sigma_{11}|} \tag{13}$$

Under loading transverse to the fibers, a composite will fail through matrix cracking and/or fiber matrix decohesion. Damage initiation is predicted by a three-dimensional adaptation of the Hashin failure criteria [21]:

$$F^{2\mathrm{T}} = \left(\frac{\langle\widehat{\sigma}_{22}\rangle}{Y_{\mathrm{is}}^{\mathrm{T}}}\right)^2 + \left(\frac{\widehat{\tau}_{12}}{S_{\mathrm{is}}^{L}}\right)^2 + \left(\frac{\widehat{\tau}_{23}}{S^{\mathrm{T}}}\right)^2 \tag{14}$$

$$F^{2\mathrm{C}} = \left(\frac{\langle-\widehat{\sigma}_{22}\rangle}{2S^{\mathrm{T}}}\right)^2 + \left[\left(\frac{Y^{\mathrm{C}}}{2S^{\mathrm{T}}}\right)^2 - 1\right]\frac{\widehat{\sigma}_{22}}{Y^{\mathrm{C}}} + \left(\frac{\widehat{\tau}_{12}}{S_{\mathrm{is}}^{L}}\right)^2 \tag{15}$$

$$F^{3\mathrm{T}} = \left(\frac{\langle\widehat{\sigma}_{33}\rangle}{Z_{\mathrm{is}}^{\mathrm{T}}}\right)^2 + \left(\frac{\widehat{\tau}_{31}}{S_{\mathrm{is}}^{\mathrm{R}}}\right)^2 + \left(\frac{\widehat{\tau}_{23}}{S^{\mathrm{T}}}\right)^2 \tag{16}$$

$$F^{3\mathrm{C}} = \left(\frac{\langle-\widehat{\sigma}_{33}\rangle}{2S^{\mathrm{T}}}\right)^2 + \left[\left(\frac{Z^{\mathrm{C}}}{2S^{\mathrm{T}}}\right)^2 - 1\right]\frac{\widehat{\sigma}_{33}}{Z^{\mathrm{C}}} + \left(\frac{\widehat{\tau}_{31}}{S_{\mathrm{is}}^{\mathrm{R}}}\right)^2 \tag{17}$$

where $Y_{\mathrm{is}}^{\mathrm{T}}$, Y^{C}, $Z_{\mathrm{is}}^{\mathrm{T}}$, and Z^{C} are the tensile and compressive strengths in the transverse and through-thickness directions, respectively, and S_{is}^{L}, S^{T}, $S_{\mathrm{is}}^{\mathrm{R}}$ are the shear strengths in the 12, 23, and 31 directions, respectively. The is subscript indicates in-situ strengths [27, 28] and $\widehat{\cdot}$ indicates a trial stress component.

Four damage variables $(d_2^{\mathrm{T}}, d_2^{\mathrm{C}}, d_3^{\mathrm{T}}, d_3^{\mathrm{C}})$ are defined that correspond to the four failure criteria. When the value of a failure criterion exceeds unity, the corresponding damage variable is updated to induce softening of the material in the relevant direction. For matrix damage, stiffness degradation is linear, and is defined by a damage evolution law of the form:

$$d = \frac{\varepsilon^{\mathrm{f}}\left(\varepsilon - \varepsilon^{0}\right)}{\varepsilon\left(\varepsilon^{\mathrm{f}} - \varepsilon^{0}\right)} \tag{18}$$

where ε^0 is the strain at damage onset, ε is the current strain, and ε^{f} represents the ultimate failure strain, given by:

$$\varepsilon^{\mathrm{f}} = \frac{2\mathcal{G}_{\mathrm{c}}}{(\sigma^0 \ell_{\mathrm{c}})} \tag{19}$$

where $\mathcal{G}_{\mathrm{c}}$ is the fracture energy of the material in the relevant direction, ℓ_{c} is the characteristic length and σ^0 is the stress at damage initiation. Note that since the shear moduli are degraded by a combination of the d_1, d_2, and d_3 variables, the model does not account for the higher toughness of the composite in shear.

Consequently, the damage variables d_2 and d_3 can be calculated as:

$$d_{\mathrm{i}} = 1.0 - (1.0 - d_{\mathrm{i}}^{T}) * (1.0 - d_{\mathrm{i}}^{C}) \quad \mathrm{i} = 2, 3 \tag{20}$$

3.3. Constitutive behavior: pure resin

Pure resin regions are assumed to be linear-elastic and isotropic with initial stiffness E_m. As such, their stiffness is degraded using a single scalar damage variable d_{m}. The compliance matrix, which is a function of the damage state, is:

$$\mathbf{H} = \frac{1}{E_{\mathrm{m}}} \begin{bmatrix} \frac{1}{(1-d_{\mathrm{m}})} & -\nu & -\nu & 0 & 0 & 0 \\ -\nu & \frac{1}{(1-d_{\mathrm{m}})} & -\nu & 0 & 0 & 0 \\ -\nu & -\nu & \frac{1}{(1-d_{\mathrm{m}})} & 0 & 0 & 0 \\ 0 & 0 & 0 & \frac{1+\nu}{(1-d_{\mathrm{m}})} & 0 & 0 \\ 0 & 0 & 0 & 0 & \frac{1+\nu}{(1-d_{\mathrm{m}})} & 0 \\ 0 & 0 & 0 & 0 & 0 & \frac{1+\nu}{(1-d_{\mathrm{m}})} \end{bmatrix} \tag{21}$$

Damage onset is predicted using the following pressure dependent loading functions adapted from the work of Liu *et al.* [29]:

$$F_{\mathrm{m}}^{\mathrm{T}} = \frac{3J_2 + I_1\left(Y^{\mathrm{C}} - Y^{\mathrm{T}}\right)}{Y^{\mathrm{C}}Y^{\mathrm{T}}} \text{ if } I_1 \geq 0 \tag{22}$$

$$F_{\mathrm{m}}^{\mathrm{C}} = -\frac{3J_2 + I_1\left(Y^{\mathrm{C}} - Y^{\mathrm{T}}\right)}{Y^{\mathrm{C}}Y^{\mathrm{T}}} \text{ if } I_1 < 0 \tag{23}$$

where I_1 is the first invariant of the stress tensor, and J_2 is the second invariant of the deviatoric stress tensor, and Y^{T} and Y^{C} are the tensile and compressive strength of the pure resin region, respectively, assumed to be equal to the transverse strengths of the unidirectional tows.

After failure initiation, damage is dissipated according to the following exponential damage evolution law following the same methodology described in Section 3.2:

$$d_{\mathrm{m}}^{\mathrm{k}} = 1 - \frac{1}{r_{\mathrm{m}}^{\mathrm{k}}} \exp\left[A_{\mathrm{m}}^{\mathrm{k}}\left(1 - r_{\mathrm{m}}^{\mathrm{k}}\right)\right] \quad \mathrm{k} = \mathrm{T}, \mathrm{C} \tag{24}$$

where $A_{\mathrm{m}}^{\mathrm{T}}$ and $A_{\mathrm{m}}^{\mathrm{C}}$ are the tensile and compressive fitting parameters used to ensure correct dissipation of fracture energy, and $r_{\mathrm{m}}^{\mathrm{T}}$ and $r_{\mathrm{m}}^{\mathrm{C}}$ represent the elastic domain thresholds under tensile and compressive loading, respectively, defined as:

$$A_{\mathrm{m}}^{\mathrm{k}} = \frac{2\ell Y^{\mathrm{k}}}{2E_{\mathrm{m}}\mathcal{G}_{\mathrm{m}}^{\mathrm{k}} - 2\ell Y^{\mathrm{k}}} \quad \mathrm{k} = \mathrm{T}, \mathrm{C} \tag{25}$$

$$r_{\mathrm{m}}^{\mathrm{T}} = \max\left\{1, \max_{s=0,t}\left\{F_M^{\mathrm{T}}\right\}, \max_{s=0,t}\left\{F_M^{\mathrm{C}}\right\}\right\} \tag{26}$$

$$r_{\mathrm{m}}^{\mathrm{C}} = \max\left\{1, \max_{s=0,t}\left\{F_M^{\mathrm{C}}\right\}\right\} \tag{27}$$

where ℓ is the constituent's characteristic length, $\mathcal{G}_{\mathrm{m}}^{\mathrm{T}}$ and $\mathcal{G}_{\mathrm{m}}^{\mathrm{C}}$ are the tensile and compressive fracture energies, and E_{m} is the bulk resin modulus. In this study the bulk resin properties were assumed to be identical to the transverse properties of a unidirectional tow. Finally the damage variable d_{m} is calculated based on the tensile and compressive damage variables:

$$d_{\mathrm{m}} = 1.0 - (1.0 - d_{\mathrm{m}}^{T}) * (1.0 - d_{\mathrm{m}}^{C}) \tag{28}$$

3.4. Implementation

The multiscale algorithm developed in the previous sections was implemented as a VUMAT subroutine in Abaqus/Explicit. The complete source code is available for download on GitHub [1]. Material properties were characterized experimentally according to the relevant standards and are listed in Table 1 with the exception of the longitudinal fracture toughnesses which were taken from the literature. $\mathcal{G}_{2-}$ was determined based on the intralaminar shear fracture toughness $\mathcal{G}_6$ and the fracture angle under pure transverse compression (53°) [23]. The undulation ratio and volume fractions of the unit cell constituents were estimated from SEM micrographs. For the press-manufactured carbon epoxy laminates used in this study the undulation ratio (as defined in Figure 4) was 0.0683.

Python scripts were developed to automate the creation of the finite element models. These scripts are publicly available on available on GitHub 1^0. Coupons were discretized with 8 node reduced integration linear solid C3D8R elements. Mesh seeds were defined such that the element sizes were approximately equal to the size of the mesoscale unit cells and the length of the undulation (≈ 1.5mm). This is the optimal element size to ensure a realistic macro-to-meso strain transformation [21]. It is worth noting that due to the automatic partitioning of the complex geometry some elements may be smaller than the mesoscale unit cell. Mesh topology was dependent on the laminate stacking sequence. Specimens were automatically meshed using swept meshes and

[1] `https://github.com/rutger-kok/composite_cdm_ap_ply`

Table 1: Mechanical properties of the SHD Composites VTC401.

Property	Value	Source
Elastic properties		
E_{11} (GPa)	124.35	ISO 527-4
$E_{22} = E_{33}$ (GPa)	7.231	ISO 527-4
$G_{12} = G_{31}$ (GPa)	3.268	ISO 14129
G_{23} (GPa)	2.638	estimated as in [30]
$\nu_{12} = \nu_{31}$ (-)	0.339	ISO 527-4
ν_{23} (-)	0.374	estimated as in [31]
Strengths		
X^{T} (MPa)	2550	ISO 527-4
X^{C} (MPa)	-1102	ASTM D 6641
$Y^{\mathrm{T}} = Z^{\mathrm{T}}$(MPa)	44	ISO 527
$Y^{\mathrm{C}} = Z^{\mathrm{C}}$(MPa)	-184	ASTM D 6641
$S^{12} = S^{31}$(MPa)	55	ISO 14129
S^{23} (MPa)	83	ISO 14130
Fracture energies		
$\mathcal{G}_1^{\mathrm{T}}$ (N/mm)	134.0	[32]
$\mathcal{G}_1^{\mathrm{C}}$ (N/mm)	95.0	[32]
$\mathcal{G}_2^{\mathrm{C}}$ (N/mm)	0.38	[33]
$\mathcal{G}^6$ (N/mm)	1.62	[33]

the advancing front algorithm. As a result of this process, the quasi-isotropic specimen mesh was largely unstructured, while the cross-ply specimens exhibited a much more regular mesh aligned with the geometry of the tows.

It is worth noting that damage localization and mesh dependency — deficiencies of classical local continuum damage mechanics models [34] — may result in the localization of damage in single element bands. It is possible to exploit the mesh dependency by aligning lamina meshes with their fiber direction to improve the accuracy of the predicted crack path [35, 36, 37, 38]. However, a systematic review of mesh alignment in composite lamina concluded that it is unnecessary for the accurate simulation of unnotched tensile tests [39]. The accumulation of damage leads to local softening behavior as the tangent stiffness becomes negative, potentially causing the nonphysical localization of deformation. To overcome this issue, each constituent's fracture toughnesses have been normalized by their characteristic length. As reported by other authors [24], this approach helps to alleviate mesh dependency, although negative tangent stiffness matrices may still induce damage localization in structured meshes. As such, it is important to consider the mesh topology when simulating the behavior of AP-PLY laminates.

The validation of the fiber tow constitutive model and a mesh convergency study is available in Appendix A. Midplane symmetry was used to reduce computational cost. Enhanced hourglass and distortion controls were enabled to improve numerical stability. Simulation runtimes for the 100 mm x 40 mm AP-PLY specimens varied from 33 mins to 600 mins running in parallel on 4 cores in a Intel Xeon E3-1230 Windows machine depending on the AP-PLY configuration.

Specimens were fully clamped at one end and a 0.5 mm/s velocity was imposed at the opposite boundary to simulate the quasi-static experiment. The internal and kinetic energy in the model were evaluated to ensure inertial forces were negligible. To avoid unrealistic element distortion resulting from the strain-softening constitutive behavior, elements were deleted from the mesh if the determinant of the deformation gradient F, i.e. the ratio of the deformed to the undeformed element volume, exceeded predefined limits, see Equation 29 [40]. The implementation of these deletion criteria improved stability and prevented simulations from aborting prematurely. It should be noted these bounds must be reviewed if the element size and/or material properties are changed, to ensure elements have dissipated all of their fracture energy before they are removed from the model.

$$\text{Delete element if} \quad 0 < \det \mathbf{F} < 0.8 \text{ or } \det \mathbf{F} > 2.5 \ . \tag{29}$$

4. Results and Discussion

4.1. Experimental results

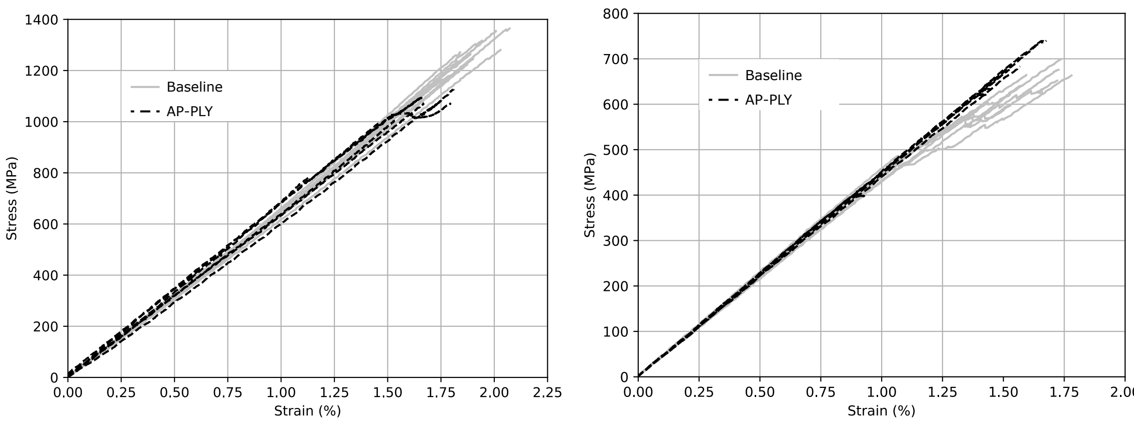

(a) Cross-ply

(b) Quasi-isotropic

Figure 6: Stress-strain response of baseline and AP-PLY composites.

Figure 6 shows representative stress-strain curves of the baseline and AP-PLY laminates and the results are summarized in Table 2. Laminate moduli were evaluated over a strain range from 0.002 to 0.008, prior to damage initiation. No significant difference was found between the initial stiffness of the AP-PLY and baseline cross-ply and quasi-isotropic panels. The result is consistent with previous studies of AP-PLY laminates which have reported minor changes in undamaged in-plane stiffness in spite of the presence of fiber crimp [6, 7, 9].

In terms of strength, the AP-PLY process was found to reduce the strength of the cross-ply laminates by as much as 16.7%. The discrepancy can be attributed to stress concentrations

Table 2: Experimental and numerical moduli and strengths for baseline and AP-PLY laminates.

Configuration	**Modulus (GPa)**		**Strength (MPa)**	
	Exp.	**FEA**	**Exp.**	**FEA**
$\mathrm{XP}_{\text{AP-PLY}}$	65.27 ± 3.53	61.71	1060.31 ± 47.55	1000.18
$\mathrm{XP}_{\text{base}}$	63.59 ± 1.23	63.26	1273.15 ± 55.61	1324.38
$\mathrm{QI}_{\text{AP-PLY}}$	44.96 ± 0.57	42.60	705.67 ± 28.85	653.62
$\mathrm{QI}_{\text{base}}$	44.56 ± 0.95	44.25	655.90 ± 29.79	643.11

induced by the through-thickness fiber undulations (see Figure 9). Post-mortem examinations of the specimens indicated that ultimate failure of the specimens occurred along tow boundaries, never splitting a tow in the direction parallel to the fibers. Additional stress concentrations were also detected near the clamped ends of the specimens due to the high gripping pressures used to prevent slippage of the large non-standard width specimens, in spite of the use of larger end tabs. This was not an issue for the baseline specimens whose dimensions conformed to the ISO standard.

In contrast to the cross-ply specimens, the averaged quasi-isotropic AP-PLY specimen strength was 7.6% higher than the baseline configuration. Notably, there was a distinct kink in the stress-strain response of the baseline specimens at a load of approximately 500 MPa. This softening behavior was not observed in the AP-PLY specimens, which exhibited linear elastic behavior up to final failure. The non-linear behavior of the quasi-isotropic baseline specimens is attributed to more extensive matrix cracking in the specimens prior to final failure, see Figure 8. In the AP-PLY specimens the ±45 and 90 degree tows do not form a continuous ply from one (clamped) end of the specimens to the other. As a result of the discontinuity of these tows, they tend not to form matrix cracks parallel to the local fiber direction within the tows themselves. Instead, these tows debond from the rest of the laminate, i.e. matrix cracks only form between tows. While the baseline cross-ply specimens also exhibit matrix cracking, they do not exhibit the same softening behavior as the baseline quasi-isotropic composite because they contain a greater proportion of load oriented plies. Similar behavior is observed in woven composites, in which extensive matrix cracking does not result in a non-linear stress strain response [41].

4.2. Numerical response: AP-PLY composites

The numerical framework described above was used to simulate the tensile response of the AP-PLY and baseline panels. Figure 7 compares the experimental and numerical stress-strain curves and results are summarized in Table 2. Laminate moduli were evaluated over a strain range from 0.002 to 0.008, prior to damage initiation. The tow region constitutive model was able to accurately predict the stiffness and strength of the baseline laminates, and their failure modes, see Fig. 8. The cross-ply specimens failed simultaneously at different points, both in the center and near the clamps. This phenomena was well captured by the numerical model. The progressive ply

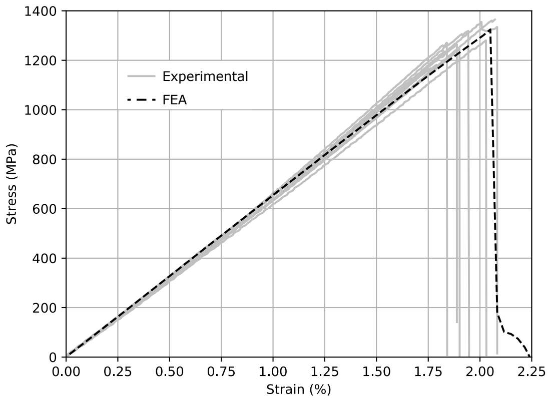

(a) XP Baseline

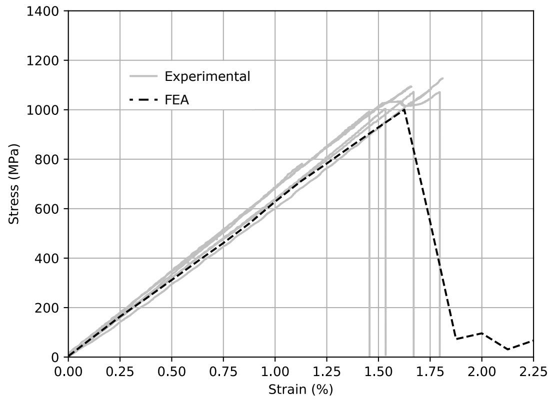

(b) XP AP-PLY

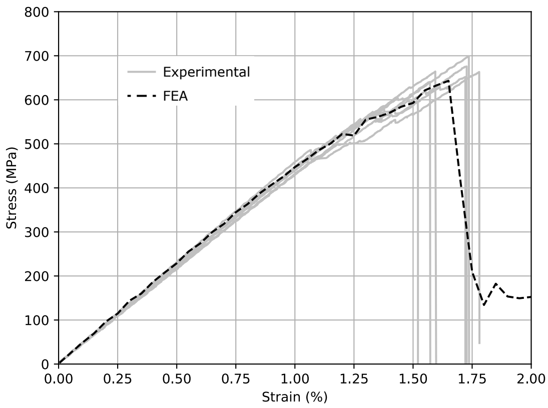

(c) QI Baseline

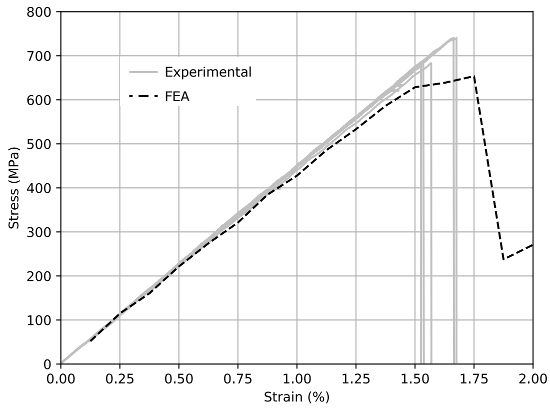

(d) QI AP-PLY

Figure 7: Comparison of experimental and predicted stress-strain curves of cross-ply (a) baseline and (b) AP-PLY and quasi-isotropic (c) baseline and (d) AP-PLY laminates.

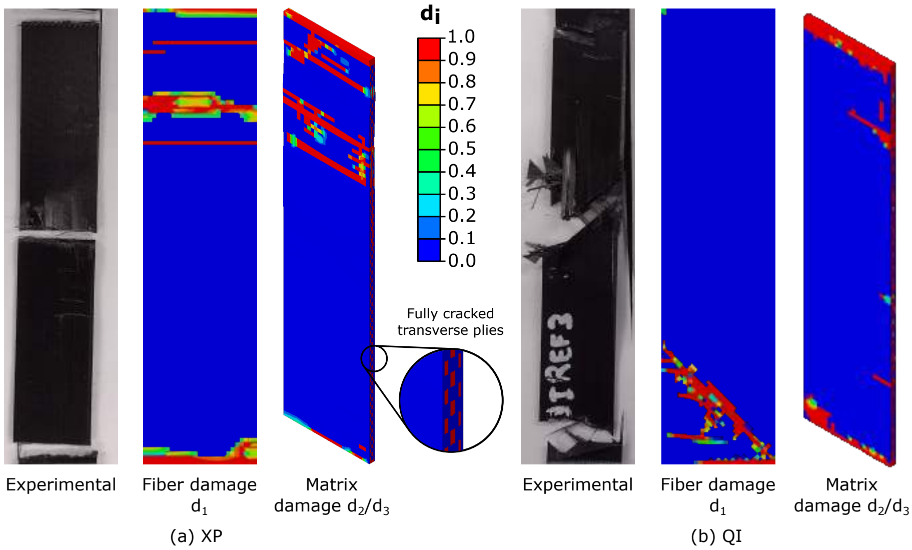

Figure 8: Numerical predictions and experimental observations of damage in cross-ply (a) and quasi-isotropic (b) baseline laminates. Note the matrix cracking in the transverse and ±45 degree tows.

failure in the quasi-isotropic specimens was also well predicted. Matrix cracking occurred at low strains in the 90° plies, followed by the ±45° laminae, spreading through the entirety of each ply. Final failure of the the specimens was caused by fiber fracture in the 0° layers, with simultaneous perpendicular and diagonal cracks.

The prediction of the mechanical response of the cross-ply AP-PLY panels was in very good agreement with the experimental results. The discrepancies between the experimental and numerical stiffness, strength, and strain to failure values amounted to 5.5%, 5.7%, and 1.8% respectively. Reasonable agreement was also obtained for the response of the quasi-isotropic panel. Stiffness was estimated by the numerical model to within 5.2% of the experimental modulus. However, as the complexity of the internal architecture increased, the numerical model tended to underestimate the strength, by approximately 7.4%.

The models presented a linear-elastic response until the onset of matrix cracking. As loads were increased, strain concentrations developed at the through-thickness tow undulations due to the differences in stiffness between adjacent tows with different out-of-plane orientation. Figure 9 compares the strain field on the surface of a cross-ply specimen (obtained using DIC) with the numerical model predictions at 1.1% nominal strain. The size and location of the strain concentrations were captured relatively accurately by the numerical model in single element bands, even using a coarse mesh.

The numerical models predicted the location and angles of the planes along which the specimens fractured, which were always aligned with the undulation regions along transverse tow boundaries. Figures 10 and 11 compare the experimentally observed fracture mechanisms with those predicted by the numerical model. Despite the relatively coarse mesh, the model was able to predict the crack paths accurately.

In the case of the quasi-isotropic laminate, failure occurred at a ±45° angle. Fiber failure also

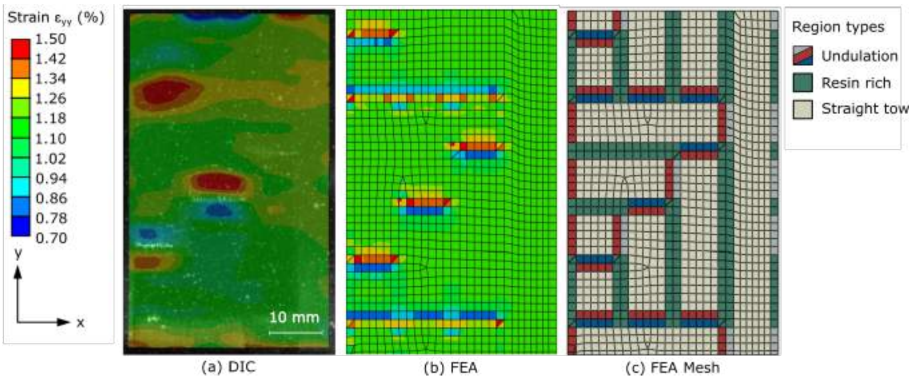

Figure 9: (a) Experimental measurements and (b) numerical predictions of the strain field on the surface of a cross-ply laminate at 1.1% nominal strain. (c) Finite element discretization divided in different unit cell regions.

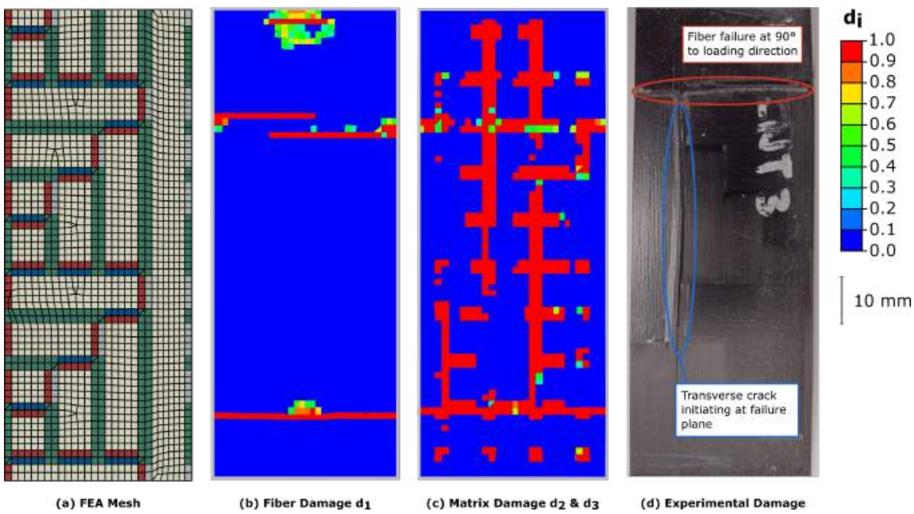

Figure 10: Numerical predictions and experimental observations of damage in cross-ply AP-PLY laminates. The finite element mesh used to discretize the top ply of the specimen is illustrated in (a). Subfigures (b) and (c) exhibit the damage envelopes corresponding to fiber damage and transverse/through-thickness damage, respectively. Deleted elements are not shown. Experimentally observed failure mechanisms are exhibited in (d).

happened on this inclined plane even in tows oriented in the loading direction, where failure would normally be expected to occur on a plane normal to the tow. In the cross-ply specimens failure occurred on a plane orthogonal to the loading direction aligned with one or more of the undulation regions. Matrix cracking was only predicted in the vicinity of the tow boundaries, instead of spread over the entirety of each transverse ply, as in the case of the baseline laminates. For example, the transverse crack which initiated on the failure plane and runs along the tow boundary was well captured by the matrix cracking criteria in the numerical model.

The accuracy of the numerical models decreased as the complexity of the internal architecture rose due to the limitations of the homogenization approach. For example, in the quasi-isotropic laminates the numerical stress-strain response diverged from the experimental results at high loads. While the stiffness of the undulations in the direction of the fibers *should* be relatively unaffected by damage to the matrix (in tension), due to the homogenization of the stresses in each undulation region, matrix damage reduced the stiffness even in the direction of the undulating fibers. An

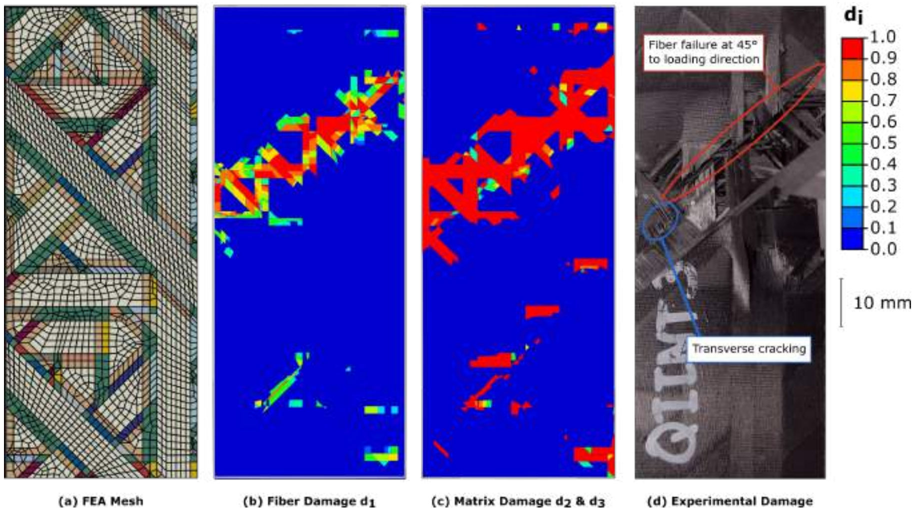

Figure 11: Numerical predictions and experimental observations of damage in quasi-isotropic AP-PLY laminates. The finite element mesh used to discretize the top ply of the specimen is illustrated in (a). Subfigures (b) and (c) exhibit the damage envelopes corresponding to fiber damage and transverse/through-thickness damage, respectively. Deleted elements are not shown. Experimentally observed failure mechanisms are exhibited in (d).

additional effect of the reduced stiffness was the premature triggering of the longitudinal failure criteria, resulting in a lower ultimate failure strength. It should be noted that the non-linear response of the resin and the shear response of the tows were not implemented. Incorporating these phenomena into the constitutive models could potentially improve strength predictions, particularly in the case of the quasi-isotropic laminates (or other composites with high resin content). However, while it is important to acknowledge the potential for reduced accuracy in the predicted strength of AP-PLY laminates with a large number of different tow orientations, the quasi-isotropic laminates studied in the present work represent the current state-of-the-art in terms of geometric complexity [6, 11, 7, 9].

Despite the aforementioned limitations, the multiscale homogenization/CDM framework presented in this study predicts the mechanical response of the AP-PLY composites with reasonable accuracy and at a reduced computational cost compared to microscale or FE^2 approaches [42, 43, 44, 45, 46]. The automated pre-processing (comprised of specimen partitioning, material property assignment, and meshing) is 6 times faster than the approach developed by Li *et al.* [18] when performed on a 4 core (Intel Xeon E3-1230) Windows machine with 16 GB of RAM. Furthermore, the use of a coarse mesh (≈1.5 mm characteristic length) to reproduce the response of the undulations drastically reduces the computational cost of the models when compared against microscale approaches that require meshes of the order of 0.07 to 0.35 mm to discretize the fiber curvature, as in studies of 3D woven and braided composites [47, 48, 44, 49, 50, 51]. While these microscale approaches might be able to replicate the stress-state in an AP-PLY composite with greater accuracy, the high number of degrees of freedom required preclude their use in the analysis of large structural components [52]. The methodology presented in this paper strikes a balance between accuracy in the prediction of the stress-strain response and computational efficiency.

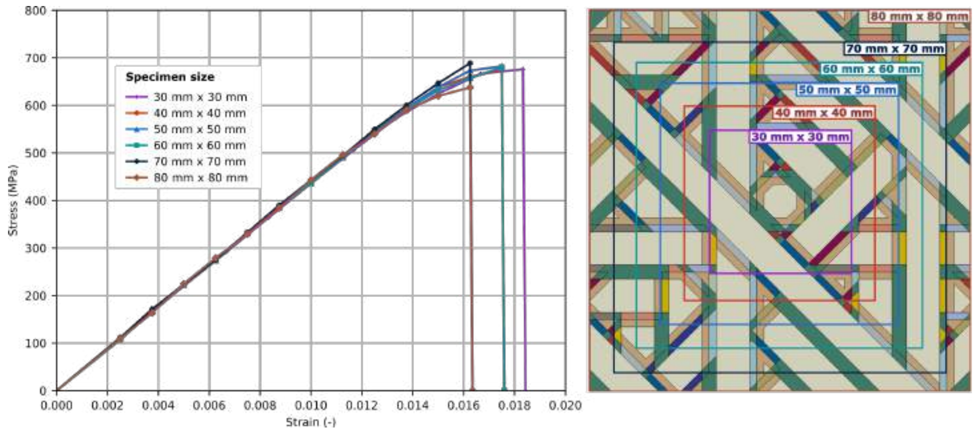

Figure 12: On the left, the numerical stress-strain curves for various sizes of QI_{AP-PLY} specimens. On the right, the corresponding specimen bounds overlaid on the mesoscale geometric idealization of a quasi-isotropic AP-PLY laminate.

4.3. Effect of specimen size

As discussed previously, the AP-PLY quasi-isotropic specimens characterized in this study contained only an “approximate RVE” as a true RVE could not be identified for laminates with this configuration. In spite of this, the experimental results exhibited low levels of variability: the coefficients of variation of the modulus and strength amounted to 1.7% and 4.9% of their mean values, respectively. To evaluate whether the dimensions of the specimen impact the numerical model results, various virtual specimens with dimensions ranging from 30×30 [mm^2] to 80×80 [mm^2] were simulated.

Figure 12 illustrates the stress-strain response of the virtual specimens. As in the experimental results, the use of an approximate RVE can be observed to have a minimal impact on laminate performance. Even the specimen size that is smaller than the approximate RVE, 30×30 [mm^2], produces results in line with the larger specimens. The mean failure stress was found to be 673 MPa with a coefficient of variation of only 2.5%. The averaged laminate stiffness is 44.21 GPa with a coefficient of variation of 1.8%. These results suggest the mechanical properties of an AP-PLY component with no strictly identifiable RVE can be determined experimentally or numerically within a reasonable scattering compatible with the requirements of primary structural components.

4.4. Effect of tow-skipping parameter

To investigate the effect of the tow skipping parameter on laminate performance, numerical models of cross-ply and quasi-isotopic laminates were generated in which either 1 or 5 tows were skipped (versus the 3 tow gap used for the experimental characterization). This parameter determines the density of the undulation regions in a laminate, hence a low tow-skipping value implies a higher number of undulations.

Laminate stiffness was unaffected by the tow skipping parameter for both the quasi-isotropic and cross-ply configuration (in agreement with the experimental results). Furthermore, the tow skipping parameter had a negligible impact on the strength of the cross-ply laminate: the maximum stresses were almost identical for all three laminate configurations (Figure 13a). In the quasi-isotropic configuration however, increasing the number of skipped tows led to an increase in laminate strength (Figure 13b). In AP-PLY laminates, the magnitude of the stress intensity factor resulting from an undulation region is dependent on the mismatch angle between the regions' micro-constituents. In the cross-ply laminate the stress intensity factor at all tow undulations was the same, and the undulations were sufficiently spread out so they did not interact. In the quasi-isotropic laminate, however, reducing the spacing of the tows resulted in interactions between the different tow undulation regions, increasing the stress intensity factor and thereby negatively affecting laminate strength.

These results show the potential of the numerical framework to analyze the influence of preforming parameters in the laminate's mechanical performance. In particular, it could be used to optimize the structural response of components manufactured by automated fiber placement subject to complex loading states, such as low-velocity impact, a potential application for the aerospace sector.

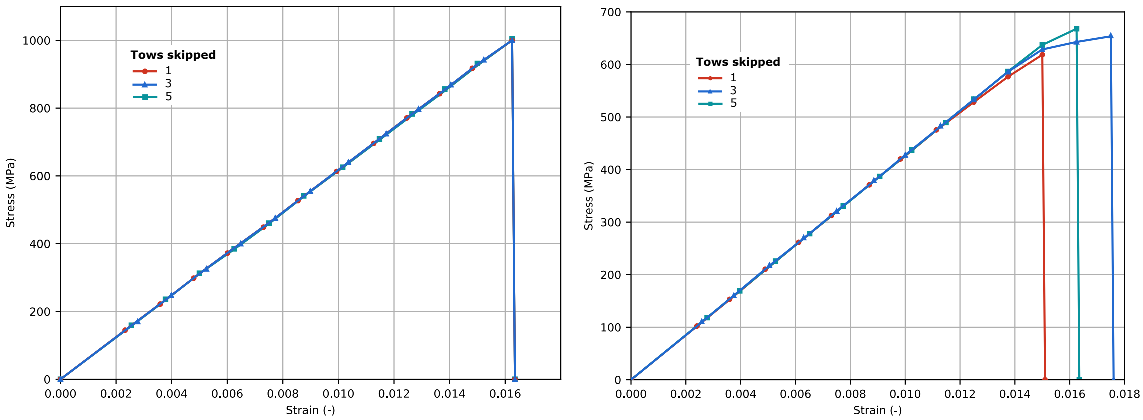

(a) Cross-ply

(b) Quasi-isotropic

Figure 13: Predicted stress-strain response of (a) cross-ply and (b) quasi-isotropic AP-PLY laminates with different numbers of tows skipped between tows placed in the same pass.

4.5. Effect of the undulation ratio

The undulation ratio used in this study was obtained using SEM micrographs. For the given material and processing method, the undulation ratio was found to be relatively constant, varying by $\pm 10\%$ from the mean value of 0.0683. A sensitivity study was conducted to determine the effect of the undulation ratio on the numerical model predictions. In the model this was implemented by changing the length of the undulation and the adjacent resin rich regions. This methodology resulted in a variation in the total fiber volume fraction of the laminate of $\pm 0.3\%$ from the initial 53.2%, which was within the bounds of the experimental scattering. The results are illustrated in Figure 14.

Laminate moduli were found to be relatively insensitive to changes in the undulation ratio. The most likely explanation for this result is that changes to the undulation ratio have two competing effects. First, as previously mentioned, increasing the undulation ratio increases the laminate FVF marginally. However, this change also increases the out-of-plane inclination of the fibers in the undulation regions, reducing the stiffness of these regions and in turn the stiffness of the laminate as whole.

In terms of strength, increasing the undulation ratio was found to have a negative impact on the strength of the laminate for both the cross-ply and quasi-isotropic laminates. As mentioned previously, increasing the undulation ratio results in larger out-of-plane fiber inclinations in the undulation regions, leading to higher stress concentrations. As a result, the longitudinal fiber failure criteria are triggered at lower nominal stresses in laminates with high undulation ratios. This effect is more significant in the cross-ply laminates where stress-concentrations are higher due to the greater ply mismatch angles. These results suggest that the AP-PLY process is best suited to thin ply composites in which the amplitude of the fiber undulation, and therefore the undulation ratio, is very small. High consolidation pressures during curing are likely to have a beneficial effect on laminate strength, for the same reason.

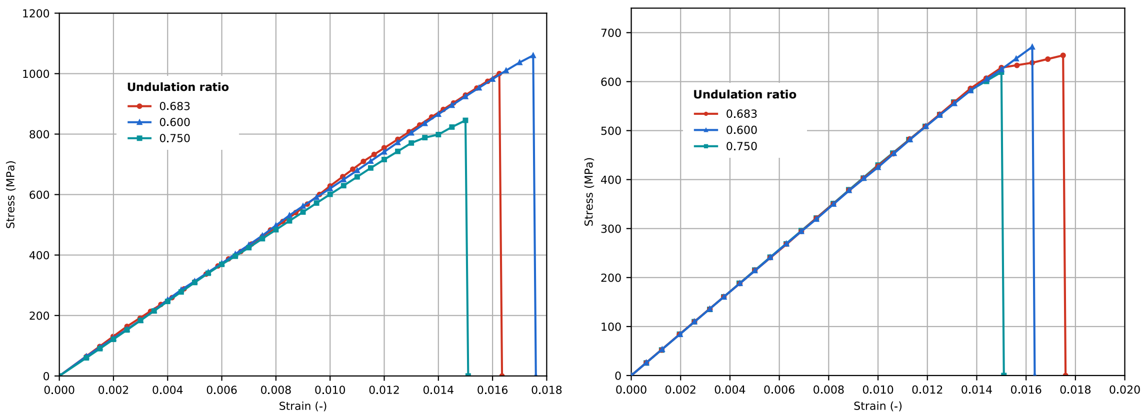

(a) Cross-ply

(b) Quasi-isotropic

Figure 14: Predicted stress-strain response of (a) cross-ply and (b) quasi-isotropic AP-PLY laminates with different undulation ratio value.

5. Conclusions

The in-plane tensile behavior of two different AP-PLY (or Advanced Placed Ply) laminates was characterized and compared with the performance of baseline conventional angle-ply composites. Due to the large RVE size, testing standards were adapted to ensure the response of the coupons was representative of the behavior of their parent laminates. Experimentally, for a given undulation ratio, the AP-PLY process was found to have a negligible impact on laminate stiffness, regardless of the AP-PLY configuration. Despite the presence of fiber crimp, the in-plane stiffness, characteristic of conventional angle-ply laminates, was retained in the AP-PLY laminates. The effect of AP-PLY preforming on laminate strength was found to depend on the layup: cross-ply laminates were found to be sensitive to the stress concentrations introduced by AP-PLY preforming, resulting in a lower strength compared with their non-AP-PLY counterparts. In contrast, the quasi-isotropic AP-PLY laminates exhibited higher strengths than the baseline laminates, possibly due to the capacity of the through-thickness reinforcement to arrest the propagation of matrix cracking and constrain it to the tow boundaries.

A novel multiscale continuum damage mechanics model was developed to predict the stress-strain response of AP-PLY composites. The AP-PLY panels were divided into three different regions: (i) straight fiber tow, (ii) undulation and (iii) resin-rich. The elements in each region acted as mesoscale unit cells. The homogenized stress state in each element at each time step was calculated based on the constitutive behavior of its micro-constituents (tow or resin). A continuum damage mechanics approach was incorporated to capture the failure of the composite. The predictive capability of the model was demonstrated through the simulation of uniaxial tensile tests. Predictions of laminate strength and stiffness were in good agreement with experimental results (within 5.5% and 7.4% of the experimental results for the cross-ply and quasi-isotropic laminates, respectively), and failure mechanisms were well captured by the modeling framework. While the multiscale approach has its limitations, the proposed model was able to provide good estimates of AP-PLY laminate performance at a reduced computational cost compared with fully microscale approaches.

The numerical framework was subsequently exploited to investigate design aspects of AP-PLY laminates. Firstly, a study on the effect of the specimen size on the laminate performance demonstrated that coherent results can be attained using "approximate" RVEs. Mechanical properties were consistent for all panel sizes and can be used for future damage tolerant design purposes, independent of the dimensions of the structural component. Secondly, a parametric study on the effect of the tow-skipping parameter in the laminate's mechanical response was conducted. It was found that increasing the number of gaps left between tows placed in the same pass increased the strength of the quasi-isotropic laminate. Cross-ply laminate strength and stiffness were unaffected. Lastly, the numerical model was used to investigate the effect of the undulation ratio on laminate strength and stiffness. Lower undulation ratios, i.e. smaller out-of-plane fiber angles, were found to increase laminate strength in both quasi-isotropic and cross-ply configurations. Stiffness was unaffected by changes to the undulation ratio.

These results show the potential of the numerical framework to optimize the fiber placement preforming process and design AP-PLY laminates with improved mechanical performance. The simulation framework can be adapted in the future to capture features of composites manufactured using automated fiber placement or filament winding, e.g. tow drops and misalignment. Subsequent studies will focus on adapting the proposed model to the simulation of more complex loading states, such as dynamic impulse and impact. The main challenge will consist of capturing complex failure modes and energy dissipation mechanisms driven by matrix cracking such as tow splitting and delamination while using a coarse mesh.

6. Declaration of Competing Interest

The authors declare that they have no known competing financial interests or personal relationships that could have appeared to influence the work reported in this paper.

7. Acknowledgments

The authors dedicate this publication to the memory of our beloved friend Claudio Lopes, who first introduced us to Nagelsmit's studies. This research was supported by the Royal Society (grant number RGS/R2/180091). The authors would like to thank James Davidson and James Quinn for providing the material characterization data. The collaboration of Amos Lim, Aidan McCusker and Justin Savage, is gratefully acknowledged. For the purpose of open access, the author has applied a Creative Commons Attribution (CC BY) licence to any Author Accepted Manuscript version arising from this submission.

8. Appendix A: Numerical model validation and mesh convergence

The fiber tow constitutive model was validated through the simulation of a baseline cross-ply specimen. Figure 15(a) compares the experimental stress-strain response of the baseline composite with the numerically predicted behavior at different mesh densities and Figure 15(b) shows the response for one single element. Numerical and experimental results were in very good agreement in terms of stiffness and strength. Failure is predicted accurately even at relatively low mesh densities. At high loads matrix damage accumulation in the numerical model softens the stress-strain response, however, this does not reduce the accuracy of the strain-to-failure prediction. The main failure mode, fiber fracture in the plies oriented with the loading direction, was effectively captured by the numerical model. The drop off in the load is the same regardless of the mesh density, indicating that the energy dissipated in the formation of a crack is independent of the element size.

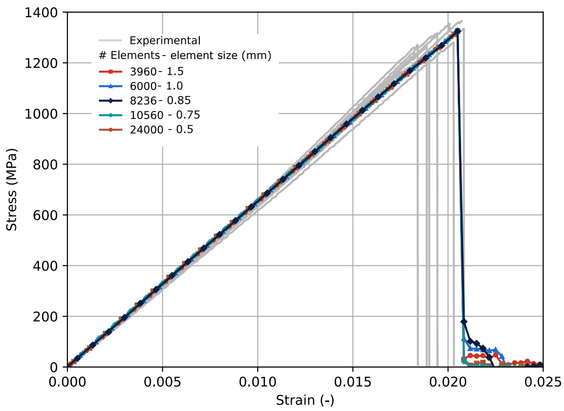

(a) Cross-ply laminate stress-strain response using different mesh densities.

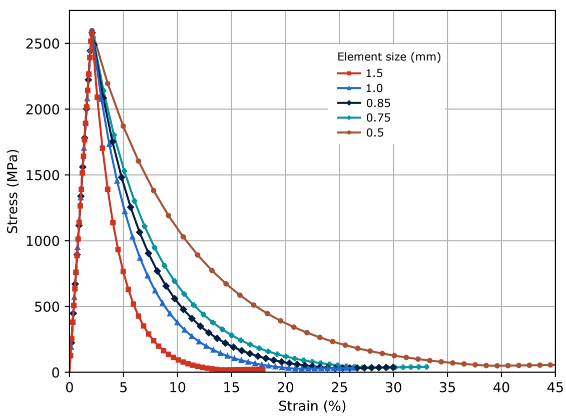

(b) Longitudinal tensile stress-strain response in single elements of different sizes.

Figure 15: Mesh convergence plots showing (a) experimental and numerical stress-strain curves for a conventional cross-ply laminate using different mesh densities and (b) stress strain response in single elements with different dimensions illustrating that energy dissipation is a function of the element volume.

References

[1] L. Zhang, X. Wang, J. Pei, and Y. Zhou, "Review of automated fibre placement and its prospects for advanced composites," *Journal of Materials Science*, vol. 55, no. 17, pp. 7121–7155, 2020.

[2] C. S. Lopes, Z. Gürdal, and P. P. Camanho, "Variable-stiffness composite panels: Buckling and first-ply failure improvements over straight-fibre laminates," *Computers and Structures*, vol. 86, no. 9, pp. 897–907, 2008.

[3] C. S. Lopes, Z. Gürdal, and P. P. Camanho, "Tailoring for strength of composite steered-fibre panels with cutouts," *Composites Part A: Applied Science and Manufacturing*, vol. 41, no. 12, pp. 1760–1767, 2010.

[4] O. Falcó, J. A. Mayugo, C. S. Lopes, N. Gascons, and J. Costa, "Variable-stiffness composite panels: Defect tolerance under in-plane tensile loading," *Composites Part A: Applied Science and Manufacturing*, vol. 63, pp. 21–31, 2014.

[5] A. P. Mouritz and B. N. Cox, "A mechanistic interpretation of the comparative in-plane mechanical properties of 3D woven, stitched and pinned composites," *Composites Part A: Applied Science and Manufacturing*, vol. 41, no. 6, pp. 709–728, 2010.

[6] M. H. Nagelsmit, *Fibre Placement Architectures for Improved Damage Tolerance*. PhD thesis, Delft University of Technology, 2013.

[7] M. D. Hoang, J.-f. Simpson, and S. V. Hoa, "Laminates With Under / Over Lacing Made By Automated Fiber Placement," *21st International Conference on Composite Materials*, no. August, pp. 1–9, 2017.

[8] B. Waddington, A. Silva-Caballero, S. Roy, W. Kennon, and P. Potluri, "Damage tolerance of Carbon/Epoxy quasi-interwoven composites subjected to low velocity impacts," *21st International Conference on Composite Materials*, no. August, pp. 20–25, 2017.

[9] P. Zivkovic, C. Ward, and G. Marengo, "Innovative preform design exploiting automated fibre placement," *ECCM 2018 - 18th European Conference on Composite Materials*, no. June, pp. 24–28, 2020.

[10] C. V. Rad, F. D. Thomas, B. Seay, and M. J. L. V. Tooren, "Manufacturing and characterization of novel clutch non-conventional fiber- reinforced composite laminates," *Composite Structures*, vol. 215, no. September 2018, pp. 454–470, 2019.

[11] C. V. Rad, F. Thomas, S. Sockalingam, and Z. Gurdal, "Low Velocity Impact Response of Hybrid Pseudo-Woven Fiber-Reinforced Composite Laminates," in *International SAMPE Technical Conference*, (Charlotte, North Carolina), SAMPE, 2019.

[12] C. V. Rad, K. Kodagali, J. Roark, D. Revilock, C. Ruggeri, R. Harik, and S. Sockalingam, "High velocity impact response of hybridized pseudo-woven carbon fiber composite architectures," *Composites Part B: Engineering*, vol. 203, no. October, p. 108478, 2020.

[13] W. Zheng and C. Kassapoglou, "Prediction of delamination onset and growth for AP-PLY composite laminates using the finite element method," *Composites Part A: Applied Science and Manufacturing*, vol. 101, pp. 381–393, 2017.

[14] W. Zheng, C. Kassapoglou, and L. Zheng, "Tailoring of AP-PLY composite laminates for improved performance in the presence of delaminations," *Composite Structures*, vol. 211, no. December 2018, pp. 89–99, 2019.

[15] L. P. Brown and A. C. Long, "Modeling the geometry of textile reinforcements for composites: TexGen," in *Composite Reinforcements for Optimum Performance (Second Edition)* (P. Boisse, ed.), Woodhead Publishing Series in Composites Science and Engineering, ch. 8, pp. 237–265, Woodhead Publishing, 2 ed., 2021.

[16] I. Verpoest and S. V. Lomov, "Virtual textile composites software WiseTex: Integration with micro-mechanical, permeability and structural analysis," *Composites Science and Technology*, vol. 65, no. 15-16 SPEC. ISS., pp. 2563–2574, 2005.

[17] A. Doitrand, C. Fagiano, F. X. Irisarri, and M. Hirsekorn, "Comparison between voxel and consistent meso-scale models of woven composites," *Composites Part A: Applied Science and Manufacturing*, vol. 73, pp. 143–154, 2015.

[18] X. Li, J. Dufty, and G. M. Pearce, "Automation of tow wise modelling for automated fibre placement and filament wound composites," *Composites Part A: Applied Science and Manufacturing*, vol. 147, no. April, p. 106449, 2021.

[19] X. Li, S. A. Brown, M. Joosten, and G. M. Pearce, "Tow Wise Modelling of Non-conventional Automated Fibre Placement Composites: Short Beam Shear Study," *Composites Part A: Applied Science and Manufacturing*, vol. 154, no. December 2021, p. 106767, 2021.

[20] R. Gerlach, C. R. Siviour, J. Wiegand, and N. Petrinic, "In-plane and through-thickness properties, failure modes, damage and delamination in 3D woven carbon fibre composites subjected to impact loading," *Composites Science and Technology*, vol. 72, no. 3, pp. 397–411, 2012.

[21] S. Shah, P. Megat-Yusoff, S. Karuppanan, R. Choudhry, and Z. Sajid, "Multiscale damage modelling of 3D woven composites under static and impact loads," *Composites Part A: Applied Science and Manufacturing*, vol. 151, no. September, p. 106659, 2021.

[22] P. Maimí, P. P. Camanho, J. A. Mayugo, and C. G. Dávila, "A continuum damage model for composite laminates: Part I – Constitutive model," *Mechanics of Materials*, vol. 39, no. 10, pp. 897–908, 2007.

[23] P. Maimí, P. P. Camanho, J. A. Mayugo, and C. G. Dávila, "A continuum damage model for composite laminates: Part II – Computational implementation and validation," *Mechanics of Materials*, vol. 39, no. 10, pp. 909–919, 2007.

[24] Z. P. Bažant and B. H. Oh, "Crack band theory for fracture of concrete," *Matériaux et Construction*, vol. 16, no. 3, pp. 155–177, 1983.

[25] Dassault Systemes, *Abaqus Analysis User's Guide*. Providence, USA: Dassault Systemes, 2019.

[26] P. P. Camanho, M. A. Bessa, G. Catalanotti, M. Vogler, and R. Rolfes, "Modeling the inelastic deformation and fracture of polymer composites-Part II: Smeared crack model," *Mechanics of Materials*, vol. 59, pp. 36–49, 2013.

[27] P. P. Camanho, C. G. Dávila, S. T. Pinho, L. Iannucci, and P. Robinson, "Prediction of in situ strengths and matrix cracking in composites under transverse tension and in-plane shear," *Composites Part A: Applied Science and Manufacturing*, vol. 37, no. 2, pp. 165–176, 2006.

[28] G. Catalanotti, P. P. Camanho, and A. T. Marques, "Three-dimensional failure criteria for fiber-reinforced laminates," *Composite Structures*, vol. 95, pp. 63–79, 2013.

[29] G. Liu, L. Zhang, L. Guo, F. Liao, T. Zheng, and S. Zhong, "Multi-scale progressive failure simulation of 3D woven composites under uniaxial tension," *Composite Structures*, vol. 208, no. June 2018, pp. 233–243, 2019.

[30] T. P. Philippidis and P. S. Theocaris, "The Transverse Poisson's Ratio in Fiber Reinforced Laminae by Means of a Hybrid Experimental Approach," 1994.

[31] R. M. Jones, *Mechanics of Composite Materials*. Boca Raton: CRC Press, 2 ed., 1999.

[32] C. Furtado, G. Catalanotti, A. Arteiro, P. J. Gray, B. L. Wardle, and P. P. Camanho, "Simulation of failure in laminated polymer composites: Building-block validation," *Composite Structures*, vol. 226, no. April, p. 111168, 2019.

[33] E. J. Pappa, J. A. Quinn, E. D. Mccarthy, J. J. Murray, J. R. Davidson, and C. M. Ó Brádaigh, "Experimental Study on the Interlaminar Fracture Properties of Carbon Fibre Reinforced Polymer Composites with a Single Embedded Toughened Film," *Polymers*, vol. 13, no. 4103, 2021.

[34] J. H. P. de Vree, W. A. M. Brekelmans, and M. A. J. van Gils, "Comparison of nonlocal approaches in continuum damage mechanics," *Computers & Structures*, vol. 55, no. 4, p. 581–588, 1995.

[35] S. Sádaba Cipriain, *High fidelity simulations of failure in fiber-reinforced composites*. PhD thesis, Polytechnic University of Madrid, 2014.

[36] O. Falcó, R. L. Ávila, B. Tijs, and C. S. Lopes, "Modelling and simulation methodology for unidirectional composite laminates in a Virtual Test Lab framework," *Composite Structures*, vol. 190, no. December 2017, pp. 137–159, 2018.

[37] C. S. Lopes, S. Sádaba, C. González, J. Llorca, and P. P. Camanho, "Physically-sound simulation of low-velocity impact on fiber reinforced laminates," *International Journal of Impact Engineering*, vol. 92, pp. 3–17, 2016.

[38] S. Sádaba, F. Martínez-Hergueta, C. S. Lopes, C. Gonzalez, and J. LLorca, "10 - Virtual testing of impact in fiber reinforced laminates," in *Woodhead Publishing Series in Composites Science and Engineering* (P. W. R. Beaumont, C. Soutis, A. B. T. S. I. Hodzic, and D. of Advanced Composites, eds.), pp. 247–270, Woodhead Publishing, 2015.

[39] S. L. Millen, Z. Ullah, and B. G. Falzon, "On the importance of finite element mesh alignment along the fibre direction for modelling damage in fibre-reinforced polymer composite laminates," *Composite Structures*, vol. 278, no. July, p. 114694, 2021.

[40] B. G. Falzon and W. Tan, "Virtual Testing of Composite Structures: Progress and Challenges in Predicting Damage, Residual Strength and Crashworthiness," in *The Structural Integrity of Carbon Fiber Composites* (P. W. R. Beaumont, C. Soutis, and A. Hodzic, eds.), ch. 24, pp. 699–743, Cham: Springer International Publishing, 1 ed., 2017.

[41] S. Daggumati, I. De Baere, W. Van Paepegem, J. Degrieck, J. Xu, S. V. Lomov, and I. Verpoest, "Local damage in a 5-harness satin weave composite under static tension: Part I - Experimental analysis," *Composites Science and Technology*, vol. 70, no. 13, pp. 1926–1933, 2010.

[42] O. Falcó, C. S. Lopes, F. Naya, F. Sket, P. Maimí, and J. A. Mayugo, "Modelling and simulation of tow-drop effects arising from the manufacturing of steered-fibre composites," *Composites Part A: Applied Science and Manufacturing*, vol. 93, pp. 59–71, 2017.

[43] M. Herráez, D. Mora, F. Naya, C. S. Lopes, C. González, and J. Llorca, "Transverse cracking of cross-ply laminates: A computational micromechanics perspective," *Composites Science and Technology*, vol. 110, pp. 196–204, 2015.

[44] S. D. Green, M. Y. Matveev, A. C. Long, D. Ivanov, and S. R. Hallett, "Mechanical modelling of 3D woven composites considering realistic unit cell geometry," *Composite Structures*, vol. 118, no. 1, pp. 284–293, 2014.

[45] F. Feyel, "Multiscale FE2 elastoviscoplastic analysis of composite structures," *Computational Materials Science*, vol. 16, no. 1-4, pp. 344–354, 1999.

[46] E. Tikarrouchine, G. Chatzigeorgiou, F. Praud, B. Piotrowski, Y. Chemisky, and F. Meraghni, "Three-dimensional FE2 method for the simulation of non-linear, rate-dependent response of composite structures," *Composite Structures*, vol. 193, no. December 2017, pp. 165–179, 2018.

[47] A. García-Carpintero, B. N. van den Beuken, S. Haldar, M. Herráez, C. González, and C. S. Lopes, "Fracture behaviour of triaxial braided composites and its simulation using a multi-material shell modelling approach," *Engineering Fracture Mechanics*, vol. 188, pp. 268–286, 2018.

[48] T. Wehrkamp-Richter, N. V. De Carvalho, and S. T. Pinho, "Predicting the non-linear mechanical response of triaxial braided composites," *Composites Part A: Applied Science and Manufacturing*, vol. 114, no. August, pp. 117–135, 2018.

[49] B. Wucher, S. Hallström, D. Dumas, T. Pardoen, C. Bailly, P. Martiny, and F. Lani, "Nonconformal mesh-based finite element strategy for 3D textile composites," *Journal of Composite Materials*, vol. 51, no. 16, pp. 2315–2330, 2017.

[50] P. Turner, T. Liu, and X. Zeng, "Collapse of 3D orthogonal woven carbon fibre composites under in-plane tension/compression and out-of-plane bending," *Composite Structures*, vol. 142, pp. 286–297, 2016.

[51] S. Dai and P. R. Cunningham, "Multi-scale damage modelling of 3D woven composites under uni-axial tension," *Composite Structures*, vol. 142, pp. 298–312, 2016.

[52] C. González, J. J. Vilatela, J. M. Molina-Aldareguía, C. S. Lopes, and J. LLorca, "Structural composites for multifunctional applications: Current challenges and future trends," *Progress in Materials Science*, vol. 89, pp. 194–251, 2017.